

Photocatalytic Activity of MOF-derived Cu₂O/Cu/C/Ag Porous Composites

Wei Chang^{a,*}, Dandan Zheng^a, Chaosheng Zhao^a and Yixin Yang^b

^aCollege of Environmental and Chemical Engineering, Xi'an Polytechnic University, Xi'an 710048, China.

^bCollege of Natural, Applied and Health Sciences, Kean University, 1000 Morris Avenue, Union, New Jersey 07083, USA.

Received 20 August 2018, revised 19 November 2018, accepted 21 November 2018.

ABSTRACT

Cu₂O/Cu/C/Ag porous composite was synthesized by heat-treatment and wet-chemical method using a typical metal-organic framework (Cu-BTC) as precursor. The samples were characterized by X-ray diffraction (XRD), scanning electron microscopy (SEM), energy dispersive spectrometry (EDS) and ultraviolet-visible spectroscopy (UV-vis). The results showed that the original structure of Cu-BTC was retained by high temperature calcination in nitrogen atmosphere. Uniform doping of Cu, C and Ag provided a triple trapping of photogenerated electron hole pairs and the Cu₂O/Cu/C/Ag exhibited an enhanced photocatalytic activity for degradation of Congo Red under visible light irradiation. Heat-treatment of the MOFs with high temperature is a facile and effective way for preparation of photocatalytic composite with desirable properties.

KEYWORDS

Photocatalyst, cuprous oxide, dye degradation, Cu-BTC.

1. Introduction

In recent years, the study of metal organic framework compounds (MOFs) has caught increasing attention. With porous structure and large specific surface area, the MOFs have important application potential in the fields of separation, sensing, catalysis and bio-pharmaceutics.²⁻⁴ As a kind of typical MOFs material, Cu-BTC was for the first time hydrothermally synthesized by Chui *et al.* using copper nitrate and benzenetricarboxylic acid as raw materials. Cu-BTC has the advantages of traditional MOFs materials such as a three-dimensional pore structure, large specific surface area (1500 m² g⁻¹) and metal active site.⁵ Since the Cu-BTC was reported, the applications of Cu-BTC in hydrogen and carbon dioxide adsorption, separation of methane mixed gas, carbon dioxide and catalytic reaction have been widely studied. Because of the high dispersion of metal ions in the MOF materials, many studies have prepared metal oxides with MOFs as the precursor.⁶⁻¹⁰

Cuprous oxide (Cu₂O), a kind of typical metal absence of p-type semiconductor, of which the band gap is from 2.0 to 2.2 eV and the hole mobility can reach 50 cm² V⁻¹ s⁻¹,¹¹⁻¹³ is a kind of ideal visible light response photocatalyst^{14,15} and can be used to induce the photocatalytic reaction under the irradiation of sunlight. It is found that Cu₂O has good stability and it can be used repeatedly. To improve the photocatalytic activity of the cuprous oxide further, the cuprous oxide-based composite materials have been designed and synthesized to promote the separation of photogenerated electron hole pairs.^{16,17} It is an effective method of doping metal materials,¹⁸⁻²⁰ non-metal materials²¹⁻²⁵ and other semiconductor materials^{26,27} to improve the photocatalytic activity of the photocatalyst. Doping by replacing the metal atoms in the lattice or in surface, or any other ways to broaden the scope of material spectral response improves its photocatalytic activity. In addition, the doping metal can improve the trapping of photogenerated electron hole pairs and reduce the recombination probability of photo-generated electrons and holes.²⁹ It has

been believed that Cu₂O has a good application prospect in photocatalytic degradation of organic pollutants, and it is expected to be a new generation of semiconductor photocatalyst after TiO₂.^{20-23,27}

Cu-BTC is a common MOF which is cheap with a wide variety of sources, but its thermal stability and reuse property is not satisfactory. In this study, a new type of photocatalytic material, Cu₂O/Cu/C/Ag was obtained using Cu-BTC as the precursor coupled with high temperature heat treatment in nitrogen atmosphere. Due to the high dispersion of metal ions in MOF materials, Cu₂O/Cu/C/Ag with Cu₂O as the main body, uniformly doping of Cu and C, and Ag loading, the photocatalytic material exhibited an enhanced photocatalytic activity under the visible light irradiation.

2. Experimental

2.1. Synthesis of Cu-BTC, Cu₂O/Cu/C and Cu₂O/Cu/Ag/C

Cu-BTC was prepared by the hydrothermal method. In a typical process, 0.869 g Cu(NO₃)₂·3H₂O was dissolved in 12 mL of distilled water and 0.426 g benzenetricarboxylic acid (H₃BTC) was dissolved in 12 mL anhydrous ethanol, then they were mixed by stirring. The resulting mixture was transferred into a 40 mL Teflon-lined stainless steel autoclave and kept at 120 °C for 12 h. After cooling to room temperature, the obtained sample was rinsed thoroughly with deionized water and ethanol for several times, and finally dried at room temperature. As a result, the violet Cu-BTC was obtained.

Cu₂O/Cu/C (CC) were obtained by calcination of the Cu-BTC in a tubular furnace at 330 °C for 2 h under the nitrogen atmosphere.

Cu₂O/Cu/C/Ag were obtained by the following two different processes described at below:

- 1) The 0.2 g CC was immersed in 100 mL 0.001 mol L⁻¹ AgNO₃ solution with magnetic stirring coupled with 500 W mercury lamp irradiation for 2 h. Then the materials were washed

* To whom correspondence should be addressed. E-mail: changwei72@163.com



with deionized water for three times and dried at room temperature. The resulting samples were marked as CCA1.

- 2) The 0.2 g Cu-BTC was immersed in 100 mL 0.001 mol L⁻¹ AgNO₃ solution with stirring for 2 h. Then the materials were collected and calcinated in a tubular furnace at 330 °C for 2 h under the nitrogen atmosphere. The obtained samples were marked as CCA2. All chemicals were of analytical grade and used without further purification.

2.2. Characterization

XRD patterns of as-prepared samples were analyzed using a Rigaku D X-ray diffractometer equipped with Cu K α irradiation ($\lambda = 0.154$ nm) at 40 kV and 40 mA. The crystallite morphological micrograph was obtained on a FEI Quanta 450 scanning electron microscope. EDS was performed on an INCA Energy X-MAX 50 scanning electron microscope. UV-vis diffused spectroscopy of the samples was recorded using a Lambda 950 (Pekin Elmer) operating between 800 nm and 200 nm wavelength, using BaSO₄ as a reference.³⁰ Photocatalytic performance was tested using the XPA-7-G8 photochemical reaction instrument.

2.3. Photocatalytic Activity Test

The photocatalytic activities of as-prepared samples were performed by the photodegradation of Congo Red under a 250 W Xenon lamp with a 420 nm cut-off filter. The distance between the lamp and tube is 6 cm. In the experiment, 3 mg of the as-prepared samples was added in 50 mL of Congo Red aqueous solution (40 mg L⁻¹). The mixture was stirred in the dark for 2 h to achieve the adsorption/desorption equilibrium before illumination. During the photoreaction, the samples were collected at regular intervals (20 min). The supernatant solution was analyzed using an UV-visible spectrophotometer (UV-2450, Shimadzu) at 500 nm. The remaining Congo Red percentage (%) after various intervals could be evaluated via Equation 1:

$$\% \text{ CR} = C/C_0 \times 100 \% \quad (1)$$

where C_0 is the initial concentration of Congo Red aqueous solution, while C is the concentration at t min.

In recycling tests, the used photocatalysts were collected and washed with ethanol and distilled water for three times. Before being reused, the photocatalysts was dried at 105 °C for 12 h.³¹

3. Results and Discussion

3.1. XRD Patterns

Figure 1 shows X-ray diffraction patterns of the as-prepared samples. The diffraction peaks of prepared Cu-BTC are nearly consistent with that of the standard Cu-BTC from 2θ of 5° to 25° and there is only a slight difference in the peak intensity (Fig. 1a). It indicated that the Cu-BTC was prepared successfully. As observed in Fig. 1b, pattern of CC mainly consist of Cu₂O and Cu diffraction peaks. The diffraction peaks appearing at 29.6° (110), 36.5° (111), 42.4° (200), 61.5° (220), 73.7° (311), 77.5° (222) are attributed to the Cu₂O (PDF#65-3288), and 43.3° (111), 50.4° (200) are attributed to the Cu (PDF# 04-0836). The patterns of CCA1 and CCA2 consist of Cu₂O, Cu and Ag diffraction peaks. The characteristic peaks located at 38.1° (111), 44.3° (200) and 64.4° (220) are attributed to Ag (PDF# 04-0783). Compared with CCA1, the diffraction peak intensity of Ag is stronger than that of CCA2, which indicates that the loaded amount of Ag in CCA2 is more than that of CCA1. The proportion of Cu₂O and Cu in CCA1 and CCA2 can be calculated according to Equation 2,

$$\text{wt}_{\text{Cu}_2\text{O}} = \frac{I_{\text{Cu}_2\text{O}} \times K_{\text{Cu}_2\text{O}}}{I_{\text{Cu}_2\text{O}} \times K_{\text{Cu}_2\text{O}} + I_{\text{Cu}} \times K_{\text{Cu}}} \quad (2)$$

$$\text{wt}_{\text{Cu}} = \frac{I_{\text{Cu}} \times K_{\text{Cu}}}{I_{\text{Cu}} \times K_{\text{Cu}} + I_{\text{Cu}_2\text{O}} \times K_{\text{Cu}_2\text{O}}}$$

where $I_{\text{Cu}_2\text{O}}$ is the integrated intensity of Cu₂O, I_{Cu} is the integrated intensity of Cu, $K_{\text{Cu}_2\text{O}}$ is the relative intensity ratio for diffraction line of Cu₂O, the value is 8.63, and K_{Cu} is the relative intensity ratio for diffraction line of Cu, the value is 6.72.³² The proportion of Cu₂O and Cu in CCA1 is about 5:3 and the proportion of Cu₂O and Cu in CCA2 is about 4:1. The content of Cu₂O in CCA2 is more than that in CCA1. There is no peak of the amorphous carbon when the 2θ is equal to 26–28° and the EDS analysis of CCA1, CCA2 shows the presence of a certain amount of carbon (Fig. 2c and Fig. 2d), suggesting that the carbon in the sample exists in amorphous phase, which is produced by the thermal decomposition of the ligand (BTC) in the nitrogen atmosphere.

3.2. SEM of the Material

Figure 2 shows the SEM images of the prepared samples. It can be seen in Fig. 2a that Cu-BTC is of typical octahedral structure.

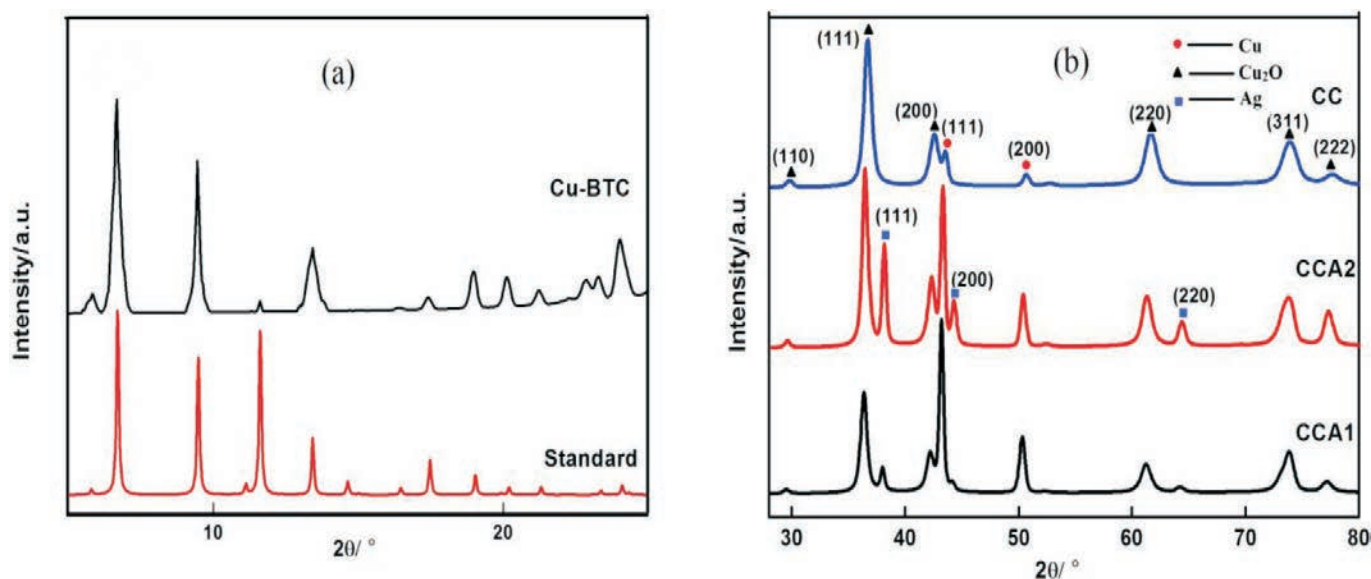


Figure 1 XRD patterns of (a) Cu-BTC, (b) CCA1, CCA2, CC.

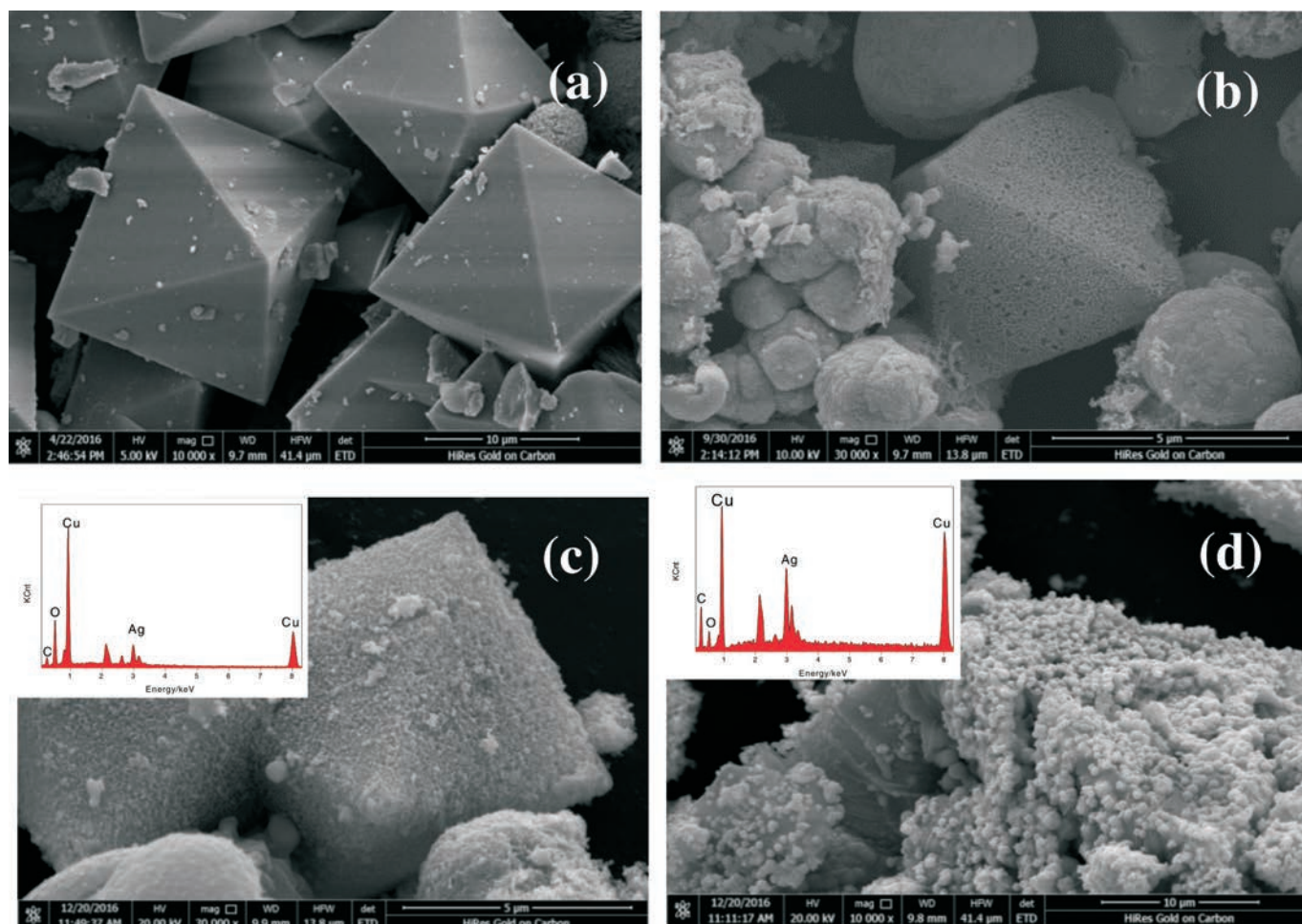


Figure 2 SEM images of the prepared samples. (a) Cu-BTC, (b) CC, (c) CCA1, (d) CCA2.

After calcination at 330 °C under nitrogen atmosphere, the basic octahedral skeleton structure was kept, which can be observed in Fig. 2b. The SEM images of $\text{Cu}_2\text{O}/\text{Cu}/\text{C}/\text{Ag}$ prepared with two different methods were shown in Fig. 2c and Fig. 2d. It can be observed obviously that the amount of loaded Ag in CCA2 is more than that in CCA1, which is consistent with the results of EDS and XRD. The EDS analysis shows that the loaded amount of Ag in CCA2 is twice of that in CCA1. Due to the higher surface area, the Cu-BTC adsorbed more Ag ions on its surface. However, with the lower surface area, the CC adsorbed less Ag ions on its surface (photo-reduction). At the same time, a certain amount of carbon appears in CCA1 and CCA2 according to the EDS analysis. The carbon content in CCA2 is significantly higher than that of CCA1 from the EDS results. Therefore, the difference of the order for calcination and silver loading leads to a great difference in silver and carbon content of $\text{Cu}_2\text{O}/\text{Cu}/\text{C}/\text{Ag}$.

3.3. Nitrogen Adsorption-Desorption

Table 1 shows the pore size and specific surface area of

Table 1 Pore Size and Specific Surface Area of Cu-BTC, CCA1 and CCA2.

Sample	Pore size /nm	Pore volume / $\text{cm}^3 \text{g}^{-1}$	BET surface area / $\text{m}^2 \text{g}^{-1}$
Cu-BTC	2.8	0.62	1537.3
CCA1	2.1	0.31	85.7
CCA2	1.9	0.22	226.5

Cu-BTC, CCA1 and CCA2. Cu-BTC has largest specific surface area ($1537.3 \text{ m}^2 \text{ g}^{-1}$). After loading Ag and calcination, CCA2 still possesses a specific surface area of $226.5 \text{ m}^2 \text{ g}^{-1}$, which is larger than CCA1. This is mainly due to the different order of Ag loading and calcination. Fig. 3 shows the nitrogen adsorption-desorption isotherms of Cu-BTC, CCA1 and CCA2. According to the IUPAC classification method, the isothermal curve of Cu-BTC belongs to the type-I isotherm curve. This type of isotherm is characterized by a rapid increase in gas sorption at low relative pressure due to the microporous filling process. Subsequent horizontal or near horizontal platforms indicate that the micropores are already filled, with little or no further adsorption occurring. It indicates that Cu-BTC has microporous structure. Both CCA1 and CCA2 belong to type II adsorption isotherm, which is generally produced by non-porous or macroporous solids. The type H4 hysteresis loops of CCA1 and CCA2 indicate that CCA1 and CCA2 contain narrow, slit-shaped pores with no adsorption at higher relative pressure areas limit range.

3.4. UV-vis Diffuse Reflectance Spectra

The UV-vis diffuse reflectance spectra of the prepared samples are shown in Fig. 4. It can be seen that Cu-BTC is not strong enough to absorb visible light and ultraviolet light. P25 absorbs strongly in the ultraviolet range, but it absorbs very weakly in the wavelength range of visible light. CCA2 has the strongest adsorption of the ultraviolet and visible light among the prepared samples. This is mainly attributed to containing more Ag and carbon in the form of amorphous phase in CCA2.

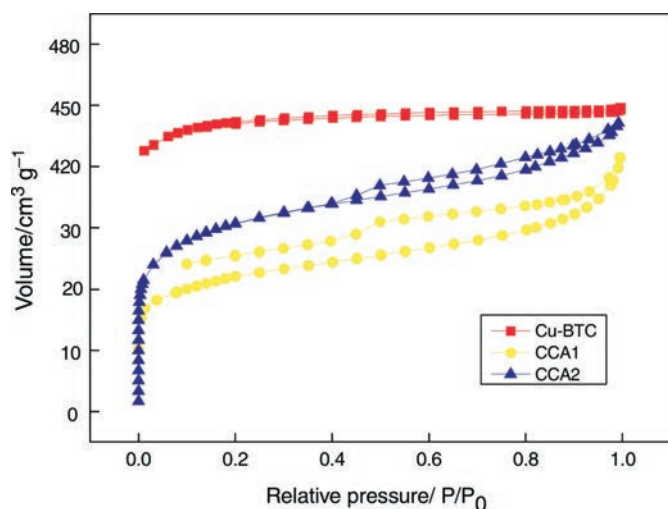


Figure 3 N_2 adsorption/desorption isotherms curves of Cu-BTC, CCA1 and CCA2.

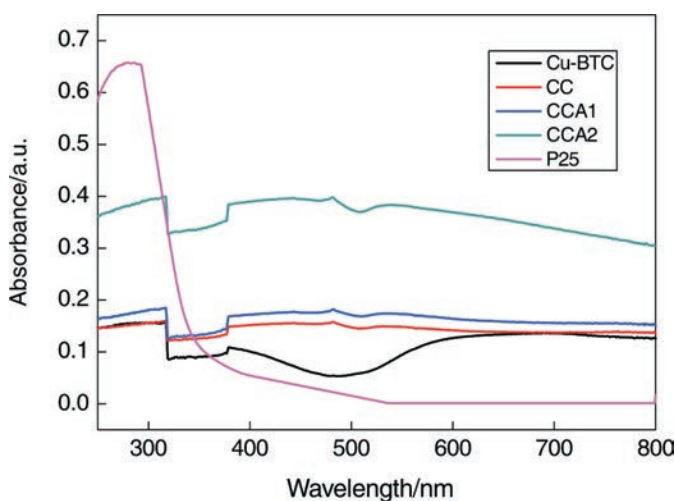
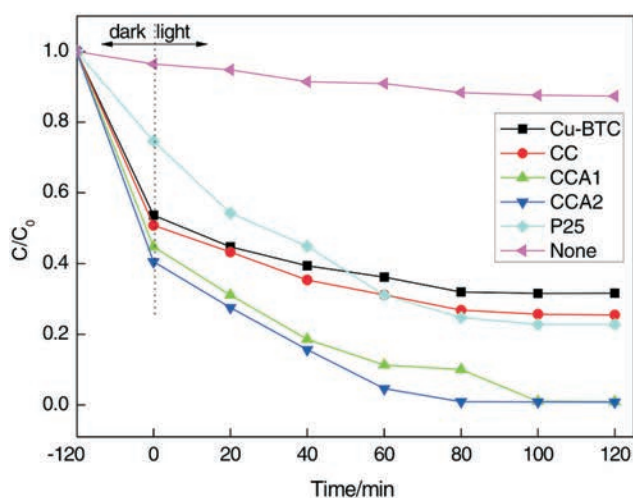
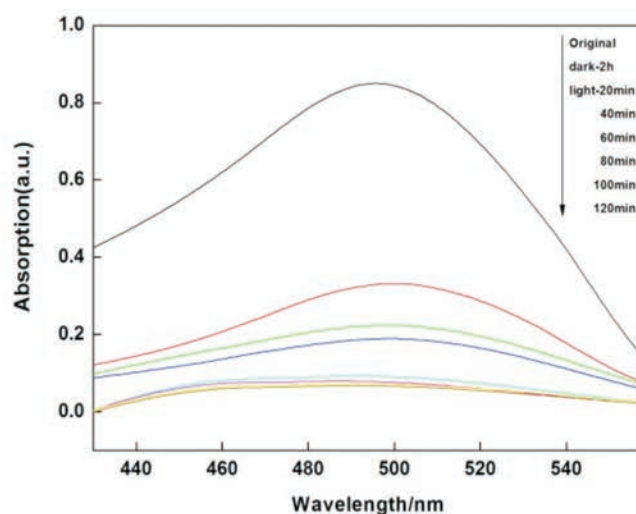


Figure 4 UV-vis spectra of Cu-BTC, CC, CCA1, CCA2 and P25.



(a)



(b)

Figure 5 (a) Photocatalytic degradation of Congo Red over CC, CCA1, CCA2, Cu-BTC and the commercial P_{25} catalyst under visible light irradiation; (b) UV-vis absorption spectra of Congo Red solution with CCA2 as the photocatalyst.

3.5. Photocatalytic Activity

Figure 5a shows the photocatalytic activities of the as-prepared samples and P_{25} catalyst for degradation of Congo Red under visible-light irradiation ($\lambda > 420$ nm). As shown in Fig. 5a, no obvious degradation of Congo Red is observed after visible light irradiation for 120 min in the absence of catalysts, indicating that the photolysis of Congo Red can be ignored. All the as-prepared samples exhibit higher adsorption efficiency for Congo Red. The photocatalytic activity of CC was better than Cu-BTC owing to the C, Cu_2O and Cu composited in it after calcination at $330^\circ C$, which improved its photocatalytic performance. After loading of Ag, the photocatalytic activity of CCA1 and CCA2 improved remarkably and the degradation efficiency for Congo Red was up to 99.1 % after irradiation for 120 min under visible light by using only 3 mg as-prepared samples. Their photocatalytic efficiencies were significantly higher than P_{25} . It also can be observed the different content of Ag, C, Cu_2O and Cu in CCA2 and CCA1 leads to slightly difference in the photocatalytic activity of CCA2 and CCA1. The absorption spectra of Congo Red degraded by using CCA2 are displayed in Fig. 5b.

To test the possibility of practical applications of the prepared samples, the stability of CCA2 was investigated. Fig. 6 shows that CCA2 keeps a relatively high stability over the successive cycles of the photocatalytic degradation of Congo Red. No significant loss of activity is observed after five successive cycles, indicating its excellent stability and potential application value in wastewater purification.

3.6. Possible Photocatalytic Mechanism

The photocatalytic mechanism of CCA1 and CCA2 is shown in Fig. 7. After loading Ag and calcination, the obtained sample CCA2 and CCA1 exhibit the most enhanced photocatalytic activity among the prepared samples. The enhanced photocatalytic activity is probably attributed to the following reasons: 1) The octahedral porous structure of Cu-BTC is retained and amorphous carbon could be obtained in CCA2 and CCA1. A certain amount of carbon provides electron traps, and after light irradiation, the photo-generated electrons by Cu_2O are more easily captured by the carbon surface, thus the recombination of electrons and holes is suppressed to a certain extent. 2) According to the metal/semiconductor heterojunction theory, the

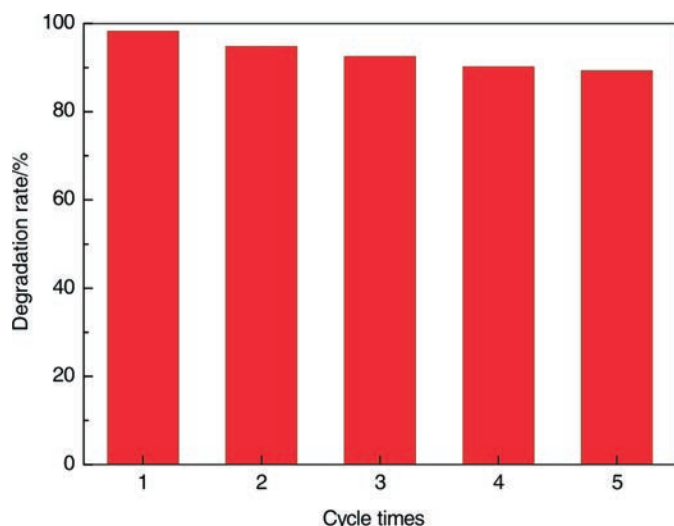


Figure 6 Reusability of the CCA2 for photodegradation of Congo Red.

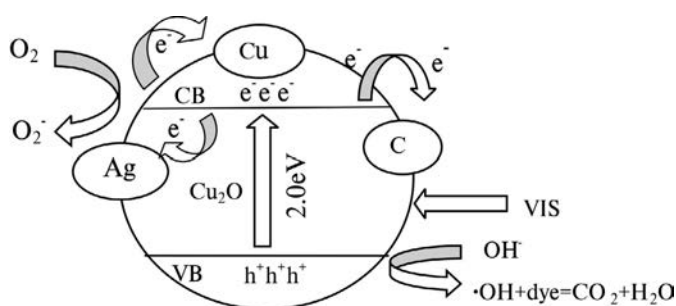


Figure 7 Diagram of CCA2 photocatalytic mechanism.

photocatalytic activity of metal/semiconductor heterojunction depends mainly on the interface defects, in which the separation efficiency of photogenic electron-hole pair can be promoted.^{33–36} The Cu in CCA2 was *in situ* generated and it can make Cu to mix uniformly with Cu₂O. Therefore, even if the Cu content is high, the fast separation of the photogenerated electrons and holes can be achieved by closely connected nanoparticles. However, as the number of Cu increases, the Cu will in turn become a new electron-hole recombination centre, leading to a reduced quantum efficiency of the materials. Therefore, CCA2 with lower Cu content exhibited better photocatalytic activity than CCA1. 3) The Ag provides abundant electron traps in CCA2, which makes it much easier for the photogenerated electrons to transfer to the surface of silver particles with lower Fermi level, which subsequently further suppresses the recombination of electrons and holes.^{37,38} Amorphous carbon, Cu and Ag in CCA1 and CCA2 exert a triple inhibitory effect, so that photogenerated electrons and holes have been effectively separated. At the same time, since the octahedral structure can adsorb organic dye molecules efficiently, the photogenerated holes can rapidly degrade the dye molecules adsorbed on the surface of the porous structure, so as to obtain excellent photocatalytic performance.

4. Conclusions

Cu₂O/Cu/C/Ag porous photocatalytic material was successfully synthesized by using Cu-BTC as the precursor. The calcination under nitrogen atmosphere retains the octahedral and porous structure of Cu-BTC. The uniform doping of Cu, C and Ag with Cu₂O suppressed the recombination of photo-generated electrons and holes effectively and thus improved the photocatalytic activity of Cu₂O/Cu/C/Ag significantly. The

Cu₂O/Cu/C/Ag is proved to be stable and reusable, and thus has potential applications in photocatalytic degradation of organic pollutants in wastewater.

Acknowledgements

This work is supported by the Science and Technology Department Research Funds of Shannxi Province, China (2018GY-131) and Research and Development Program of Beilin Distric, Xi'an, China (GX1808).

References

- Z. Wu, X. Yuan, J. Zhang, H. Wang, L. Jiang and G. Zeng, Photocatalytic decontamination of wastewater containing organic dyes by metal-organic frameworks and their derivatives. *ChemCatChem*, 2017, 9, 41–64.
- M. Yoon, R. Srirambalaji and K. Kim, Homochiral metal-organic frameworks for asymmetric heterogeneous catalysis, *Chem. Rev.*, 2012, 112, 1196–1231.
- O.K. Farha and J.T. Hupp, Rational design, synthesis, purification, and activation of metal-organic framework materials, *Accounts Chem. Res.*, 2010, 43, 1166–1175.
- M. Meilikhov, K. Yussenko and D. Esken, Metals@MOFs-loading MOFs with metal nanoparticles for hybrid functions, *Eur. J. Inorg. Chem.*, 2010, 24, 3701–3714.
- H.B. Aiyappa, P. Pachfule and R. Banerjee, Porous carbons from nonporous MOFs: influence of ligand characteristics on intrinsic properties of end carbon, *Cryst. Growth. Des.*, 2013, 13, 4195–4199.
- W. Cho Krafft, C. Wang Y.H. Lee and H.J. Lee, Systematic transformation of coordination polymer particles to hollow and non-hollow In₂O₃ with predefined morphology, *Chem. Commun.*, 2009, 31, 4756–4758.
- K.E. Krafft, C. Wang and W.B. Lin, Metal-organic framework template synthesis of Fe₂O₃/TiO₂ nanocomposite for hydrogen production. *Adv. Mater.*, 2012, 24, 2014–2018.
- L. Peng, J.L. Zhang and Z.M. Xue, Large-pore mesoporous Mn₃O₄ crystals derived from metal-organic frameworks, *Chem. Commun.*, 2013, 49, 11695–11697.
- Y.Y. Liang, Y.G. Li, H.L. Wang and H.J. Dai, Strongly coupled inorganic/nanocarbon hybrid materials for advanced electrocatalysis, *J. Am. Chem. Soc.*, 2013, 135, 2013–2036.
- W. Xia, R.Q. Zou and L. An, Metal-organic framework route to in-situ encapsulation of Co@Co₃O₄@C core@shell nanoparticles into porous carbon matrix for oxygen reduction, *Environ. Sci.*, 2015, 8, 568–576.
- Y. Yu, L. Zhang and J. Wang, Preparation of hollow porous Cu₂O microspheres and photocatalytic activity under visible light irradiation, *Nanoscale Res. Lett.*, 2012, 7, 347–352.
- A. Roos, T. Chibuye and B. Karlsson, Properties of oxidized copper surfaces for solar applications, *Sol. Energ. Mat.*, 1983, 7, 453–465.
- K. Akimoto, S. Ishizuka and M. Yanagita, Thin film deposition of Cu₂O and application for solar cells, *Sol. Energ.*, 2006, 80, 715–722.
- H. Yang, J. Ouyang and A. Tang, Electrochemical synthesis and photocatalytic property of cuprous oxide nanoparticles, *Mater. Res. Bull.*, 2006, 41, 1310–1318.
- M.D. Susman, Y. Feldman and A. Vaskevich, Chemical deposition of Cu₂O nanocrystals with precise morphology control, *ACS Nano*, 2014, 8, 162–174.
- Y. Wang, S. Li, H. Shi and K. Yu, Facile synthesis of p-type Cu₂O/n-type ZnO nano-heterojunctions with novel photoluminescence properties, enhanced field emission and photocatalytic activities, *Nanoscale*, 2012, 24, 7817–7824.
- A. Wang, X. Li and Y. Zhao, Preparation and characterizations of Cu₂O/reduced graphene oxide nanocomposites with high photocatalytic performances, *Powder Technol.*, 2014, 261, 42–48.
- W. Zhang, X. Yang and Z. Qian, One-pot room temperature synthesis of Cu₂O/Ag composite nanospheres with enhanced visible-light-driven photocatalytic performance, *Ind. Eng. Chem. Res.*, 2014, 53, 16316–16323.
- Y. Wang, H. Fang, Y. Zheng, R. Ye, X. Tao and J. Chen, Controllable assembly of well-defined monodisperse Au nanoparticles on hierarchical ZnO microspheres for enhanced visible-light-driven photocatalytic and antibacterial activity, *Nanoscale*, 2015, 7, 19118–19128.

- 20 B. Zhou, Z. Liu and H. Wang, Experimental study on photocatalytic activity of Cu₂O/Cu nanocomposites under visible light, *Catal. Lett.*, 2009, **132**, 75–80.
- 21 A. Eivazihollagh, M. Norgren, C. Dahlström and H. Edlund, Controlled synthesis of Cu and Cu₂O NPs and incorporation of octahedral Cu₂O NPs in cellulose II films, *Nanomaterials*, 2018, **238**, 1–11.
- 22 M.Y. Wang, J.R. Huang and Z.W. Tong, Reduced graphene oxide–cuprous oxide composite via facial deposition for photocatalytic dye-degradation, *J. Alloy. Compd.*, 2013, **568**, 26–35.
- 23 W.A. Wang, Q. Shi and Y.P. Wang, Preparation and characterization of iodine-doped mesoporous TiO₂ by hydrothermal method, *Appl. Surf. Sci.*, 2011, **257**, 3688–3696.
- 24 Y.H. Tang, Z. Hang and W. Yin, Facile fabrication of nitrogen-doped zinc oxide nanoparticles with enhanced photocatalytic performance, *Micro Nano Lett.*, 2015, **10**, 432–434.
- 25 Y.H. Lin, C.H. Weng, A.L. Srivastav, Y.T. Lin and J.H.T. Zeng, Facile synthesis and characterization of N-doped TiO₂ photocatalyst and its visible-light activity for photo-oxidation of ethylene, *J. Nanomater.*, 2015, **3**, 311–317.
- 26 Y.Z. Zheng, Y.Y. Xu, H.B. Fang, Y. Wang and X. Tao, Au nanoparticle homogeneously decorated C@TiO₂ for enhanced visible-light-driven photocatalytic activity, *RSC Adv.*, 2015, **5**, 103790–103796.
- 27 J. Li, L. Liu and Y. Yu, Preparation of highly photocatalytic active nano-size TiO₂-Cu₂O particle composites with a novel electrochemical method, *Electrochem. Commun.*, 2004, **6**, 940–943.
- 28 C.C. Hu, J.N. Nian and H. Teng, Electrodeposited p-type Cu₂O as photocatalyst for H₂ evolution from water reduction in the presence of WO₃, *Solar Energy Materials & Solar Cells*, 2008, **92**, 1071–1076.
- 29 V. Subramanian, E.E. Wand and P.V. Kamat, Catalysis with TiO₂/Gold nanocomposites. effect of metal particle size on the fermi level equilibration, *J. Am. Chem. Soc.*, 2004, **126**, 4943–4950.
- 30 G. Yang, Q. Zhang, W. Chang and W. Yan, Fabrication of Cd_{1-x}Zn_xS/TiO₂ heterostructures with enhanced photocatalytic activity, *J. Alloy. Compd.*, 2013, **580**, 29–36.
- 31 B. Li, Z. Sun, Y. Xue, G. Yao and S. Zheng, A facile synthesis of g-C₃N₄/TiO₂ hybrid photocatalysts by sol-gel method and its enhanced photodegradation towards methylene blue under visible light, *Adv. Powder Technol.*, 2016, **27**, 330–337.
- 32 S.S. Jaroudi, A. Hamid and A.R.I. Mohammed, Use of X-ray powder diffraction for quantitative analysis of carbonate rock reservoir samples. *Powder Technol.*, 2007, **175**, 115–121.
- 33 P. Zhang, T. Wang and H. Zeng, Design of Cu-Cu₂O/C₃N₄ nano-component photocatalysts for hydrogen evolution under visible light irradiation using water-soluble erythrosin B dye sensitization. *Appl. Surf. Sci.*, 2016, **391**, 404–414.
- 34 J.F.D. Brito, A.R. Araujo and K. Rajeshwar, Photoelectrochemical reduction of CO₂ on Cu/Cu₂O films: product distribution and pH effects, *Chem. Eng. J.*, 2015, **264**, 302–309.
- 35 W. Chen, Z. Fan and Z. Lai, Synthesis of core-shell heterostructured Cu/Cu₂O nanowires monitored by in situ XRD as efficient visible-light photocatalysts, *J. Mater. Chem. A*, 2013, **1**, 13862–13868.
- 36 C. Zhou, Z. Liu and H. Zhang, One-pot synthesis of Cu₂O/Cu self-assembled hollow nanospheres with enhanced photocatalytic performance, *J. Nanomater.*, 2014, **2014**, 1–8.
- 37 J. Yang, Z. Li, C. Zhao, Facile synthesis of Ag-Cu₂O composites with enhanced photocatalytic activity. *Mater. Res. Bull.*, 2014, **60**, 530–536.
- 38 S. Yang, S. Zhang and H. Wang, Controlled preparation of Ag-Cu₂O nanocorncocks and their enhanced photocatalytic activity under visible light, *Mater. Res. Bull.*, 2015, **70**, 296–302.